Accepted Manuscript

Improving upconversion emission of $NaYF_4$:Yb^{3+}, Er^{3+} nanoparticles by coupling Au nanoparticles and photonic crystals: The detection enhancement of Rhodamine B

Yingjin Ma, Jialun Zhu, Zhengwen Yang, Hailu Zhang, Jianbei Qiu, Zhiguo Song

PII: S0925-8388(19)30803-5

DOI: https://doi.org/10.1016/j.jallcom.2019.02.331

Reference: JALCOM 49763

To appear in: *Journal of Alloys and Compounds*

Received Date: 4 December 2018

Revised Date: 18 January 2019

Accepted Date: 28 February 2019

Please cite this article as: Y. Ma, J. Zhu, Z. Yang, H. Zhang, J. Qiu, Z. Song, Improving upconversion emission of $NaYF_4$:Yb^{3+}, Er^{3+} nanoparticles by coupling Au nanoparticles and photonic crystals: The detection enhancement of Rhodamine B, *Journal of Alloys and Compounds* (2019), doi: https://doi.org/10.1016/j.jallcom.2019.02.331.

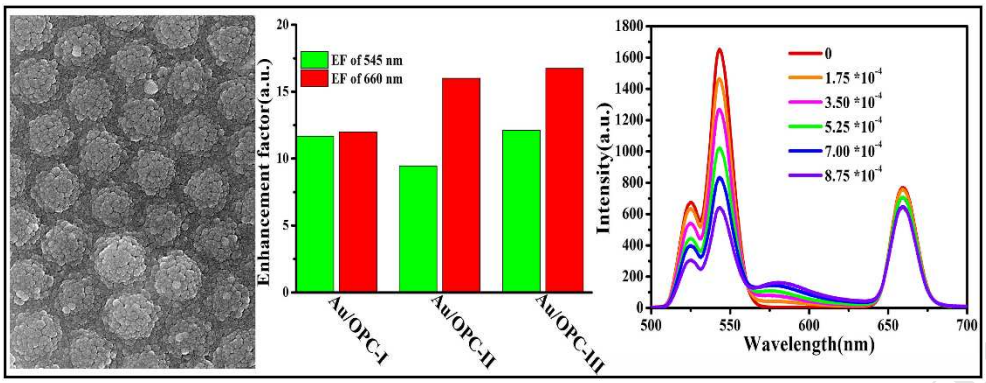

Improving upconversion emission of $NaYF_4$:Yb^{3+}, Er^{3+} nanoparticles by coupling Au nanoparticles and photonic crystals: the detection enhancement of Rhodamine B

Yingjin Ma[1], Jialun Zhu[2], Zhengwen Yang[1], Hailu Zhang[1], Jianbei Qiu[1], Zhiguo Song[1]*

[1]College of Materials Science and Engineering, Kunming University of Science and Technology, Kunming, 650093, China; [2]Department of Nuclear Medicine, Tumor Hospital of Yunnan Province, Kunming Medical University, Kunming, 650118, China

**Corresponding Email: yangzw@kmust.edu.cn; Jialun Zhu is the co-first author*

Abstract: The upconversion (UC) nanoparticles (NPs) based sensor exhibits the potential application for the detection of dyes, heavy metal ions and DNA, et al. However, the application of upconversion NPs based sensor was limited due its low UC luminescence intensity. In the present work, the SiO_2 opal photonic crystals were prepared by the self-assembly technology. After infiltration of SiO_2 opal by the transparent chloroauric acid solution and the following sintering at the high temperature, the Au NPs/opal hybrids were prepared. The Au NPs/opal hybrids result in the enhancement of excited electric field, which can be served as the template of UC emission enhancement of $NaYF_4$:Yb^{3+}, Er^{3+} NPs exited at the 980 nm. The corresponding maximum UC emission enhancement was about 17-fold. The detection of Rhodamine B was realized by monitoring the changing of green UC intensity of $NaYF_4$:Yb^{3+}, Er^{3+} NPs. In comparison with pure $NaYF_4$:Yb^{3+}, Er^{3+} NPs, the sensor sensitivity of $NaYF_4$:Yb^{3+}, Er^{3+} NPs deposited on the Au NPs/opal hybrid was increased by about the 35-factors, which exhibits a low detection limit of 164 μM and a high sensitivity of 1.15 μM^{-1}. The present work demonstrated that this solid sensor exhibits potential applications in heavy metal ions and DNA, et al.

Keyword: Upconversion luminescence; $NaYF_4$:Yb^{3+}, Er^{3+} nanoparticles; Rhodamine B sensing; Au nanoparticles/opal hybrids

1. Introduction

With the development of industries and economic, the organic rhodamine B dye (RhB) was widely used in the food, printing, textile and water tracer fluorescent [1-4]. At present, lots of investigations demonstrated that the RhB has toxicity and carcinogenicity to human health and can pollute the water source [5-7]. However, the RhB is still applied in the textile and food, etc. because of its low cost and bright coloration [8, 9]. Thus, the detection of RhB in various fields such as the food and water is very important and necessary. Now, for the detection method of RhB, the high-performance liquid chromatography, surface-enhanced resonance Raman scattering, electrochemistry and ultraviolet-visible spectrophotometry method were extensively used [10-12]. These detection approaches are complex and their applications were limited.

Upconversion (UC) luminescent nanoparticles (NPs), which convert long wavelength photons with low energy into a short wavelength photon with high energy, have aroused much attention due to their wide applications in the various fields such as the biological imaging, therapeutics and solar cells, etc. [13-16]. In recent years, the UC NPs exhibits the potential application in the sensors for the detection of dyes, heavy metal ions and DNA, et al [17-21]. However, the UC luminescent process mainly arises from the 4f-f forbidden transition of rare earth (RE) ions, resulting in a lower UC emission efficiency due to the small absorption and emission cross section. For example, the $NaYF_4$:Yb^{3+}, Er^{3+} NPs are considered as one of the most efficient UC materials in the previous investigations. However, its UC efficient is only up to

0.3%, which limit their applications as the sensor. Thus, it is significant to improve the UC luminescence of $NaYF_4$:Yb^{3+}, Er^{3+} NPs. To solve the problems, many methods such as synthesis of core-shell structure, host selection and surface coating et al have been developed to improve the UC emission of $NaYF_4$:Yb^{3+}, Er^{3+} NPs. Located surface plasmons resonance (LSPR) of metal NPs such as Au and Ag has been widely used to enhance UC luminescence of $NaYF_4$:Yb^{3+}, Er^{3+} NPs in previous investigations [22-24]. For the UC luminescent enhancement based on the LSPR of metal NPs, it is well-known that the 980 nm excitation light or UC luminescence wavelength is needed to overlap with the LSPR of Au or Ag NPs to obtain the larger UC luminescent enhancement of $NaYF_4$:Yb^{3+}, Er^{3+} NPs. However, in general, the LSPR of Au or Ag NPs is in the visible light region. It is relatively difficulty for the preparation of Au or Ag NPs with the LSPR of 980 nm. Therefore, a new approach based on the coupling between photonic crystals and metal NPs with the visible LSPR were developed in order to obtain larger UC luminescent enhancement [25, 26]. For example, the inverse opal photonic crystal including Ag NPs with the visible LSPR of Au or Ag NPs was applied to improve the UC luminescence of $NaYF_4$:Yb^{3+}, Er^{3+} NPs. However, the $NaYF_4$:Yb^{3+}, Er^{3+} NPs can be entered into the macrospore in the inverse opal structure, which cause the suppression the UC luminescent. Thus, the maximum enhancement factor of UC luminescence was only 6.3 factor [27]. Additionally, there have few investigations on the detection of Rhodamine B by the UC NPs/Au/PC hybrids. In this work, the SiO_2 opal photonic crystals (OPCs) were prepared by self-assembly technology. After infiltration of OPCs by the transparent chloroauric

acid solution and the following sintering at the high temperature, the Au NPs/OPCs hybrids were obtained. The $NaYF_4$:Yb^{3+}, Er^{3+} NPs were deposited on the surface of Au/OPCs hybrids. The influence of coupling metal NPs with photonic crystals on the UC luminescence of $NaYF_4$:Yb^{3+}, Er^{3+} NPs has been investigated. The detection of RhB was investigated by monitoring the changing of the green UC intensity of UC NPs/Au/PC hybrids. The low detection limit and high detection sensitivity of Rh B was obtained by the UC NPs/Au/OPCs hybrids.

2. Experimental

2.1 Synthesis of $NaYF_4$:20%Yb^{3+}, 2%Er^{3+} NPs.

High purity (99.99%) Yb_2O_3, Y_2O_3, Er_2O_3, and analytical reagent grade 1-octadecylene, NaOH, oleic acid, NH_4F were used as raw materials to synthesize $NaYF_4$:Yb^{3+}, Er^{3+} NPs. The hexagonal phase $NaYF_4$:Yb^{3+}, Er^{3+} NPs were prepared by co-precipitation method according to the literatures [28]. Firstly, the RE_2O_3 (RE^{3+}= Y^{3+}, Yb^{3+} and Er^{3+}) were dissolved in the hot HCl solution to form corresponding $RECl_3$ compounds, and then the $RECl_3$ compounds were dissolved in deionized water to form the 0.2 mol/L $RECl_3$ solution. The 1.56 mL YCl_3, 0.4 mL $YbCl_3$ and 0.04 mL $ErCl_3$ was added into the mixture of 12 mL 1-octadecylene and 8 mL oleic acid in a three-necked flask. The mixture was heated to 150 ^oC for 40 min to remove water with the argon gas under the stirring. After cooling to room temperature, the 2 mL NaOH and 6.6 mL NH_4F were added into the mixture, which was heated to 50 ^oC for 30 min. Subsequently, the solution was heated to the 100 ^oC for 10 min to remove methanol, then it was heated at the 300 ^oC for 50 min under the argon shield. The

resulting $NaYF_4$:Yb^{3+}, Er^{3+} NPs was obtained by centrifuging three times and dispersing in cyclohexane.

2.2 Fabrication of $NaYF_4$:Yb^{3+}, Er^{3+} NPs/Au/OPC hybrids.

Monodisperse SiO_2 microspheres with diameter of 250, 300 or 460 nm were used to fabricate three-dimensional ordered OPCs on the quartz substrates through vertical deposition method as the previous work [29]. The OPCs prepared by the 250, 300 or 460 nm SiO_2 microspheres were denoted as the OPC-I, OPC-II and OPC-III, respectively. The voids of OPC-I, OPC-II and OPC-III were infiltrated by using the 0.05M $HAuCl_4$ solution, respectively. After sintering at 450 ^{o}C for 4h in air furnace, the Au NPs and OPC-I~III composites were obtained, denoting as the Au/OPC-I, Au/OPC-II and Au/OPC-III, respectively. For the comparison, the same $HAuCl_4$ solution was deposited on the pure quartz substrate without the OPCs and was sintered at the same temperature and time, which was denoted as the Au/Q. The as-prepared $NaYF_4$:Yb^{3+}, Er^{3+} NPs were spin-coated on the pure quartz (denoted as Q), Au/Q, Au/OPC-I~III substrates, and the $NaYF_4$ NPs/Au/OPC-I~III hybrids were obtained. Scheme 1 shows the preparation processes of $NaYF_4$ NPs/Au/OPC-I~III hybrids.

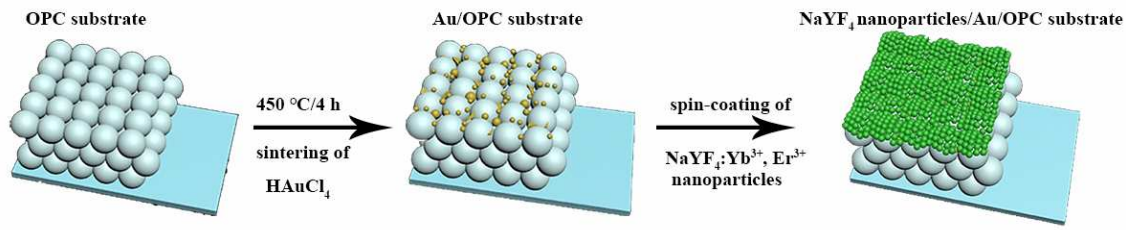

Scheme 1 the preparation processes of $NaYF_4$ NPs/Au/OPC hybrids

The RhB was dissolved in the various volume ethanol to form $1.75*10^{-4}$,

$3.5*10^{-4}$, $5.25*10^{-4}$, $7*10^{-4}$ and $8.75*10^{-4}$ M solutions, respectively. Then, the 2 μL RhB solution with the different concentration was added into the $NaYF_4$ NPs/Au/OPC-III hybrids and dried on the oven for the detection investigation of RhB.

2.3 Structure and optical characterization.

The crystal phase and morphology of $NaYF_4$:Yb^{3+}, Er^{3+} NPs were detected by an X-ray diffraction diffractometer quipped with Cu Kα radiation and transmission electron microscopy (TEM, JEOL 2100), respectively. The morphology of OPC-I~III, Au/OPC-I~III and $NaYF_4$ /Au/OPC-I~III hybrids were measured using a field emission scanning electron microscopy (FESEM, QUANTA 650). To further investigate the distribution of Au NPs on the OPC-I~III, the transmission electron microscopy and energy dispersive X-ray analysis image of Au/OPC OPC-I~III hybrids were obtained by transmission electron microscopy (TEM, JEOL 2100). The absorption spectra were taken using a HITACHIU-4100 spectrophotometer. The UC emission spectra of samples were characterized by a HITACHI F-7000 spectrophotometer with an excitation of 980 nm.

3. Results and discussions

3.1 Morphology and absorption property of $NaYF_4$ NPs/Au/OPC-I~III hybrids

Figure 1 (a) is the XRD pattern of $NaYF_4$ NPs. It is clearly that all peaks are well-indexed to the standard PDF card (JCPDS No. 16-0334), indicating that the prepared $NaYF_4$ NPs are pure hexagonal phase. Figure 1 (b) shows the TEM image of $NaYF_4$ NPs, depicting the monodisperse and inerratic morphology of $NaYF_4$ NPs with average diameter of 25 nm. The high resolution TEM image of $NaYF_4$ NPs exhibits the clear lattice fringes as shown in Figure 1 (c). The space of two adjacent

lattice fringes is 0.3 nm, which is consistent with the (110) plane of hexagonal $NaYF_4$. The selected area electron diffraction (SAED) pattern was observed in Figure 1 (d). The diffraction rings are marked as (200), (111), (201), (210) and (002), which further demonstrated that the $NaYF_4$ NPs is the hexagonal phase.

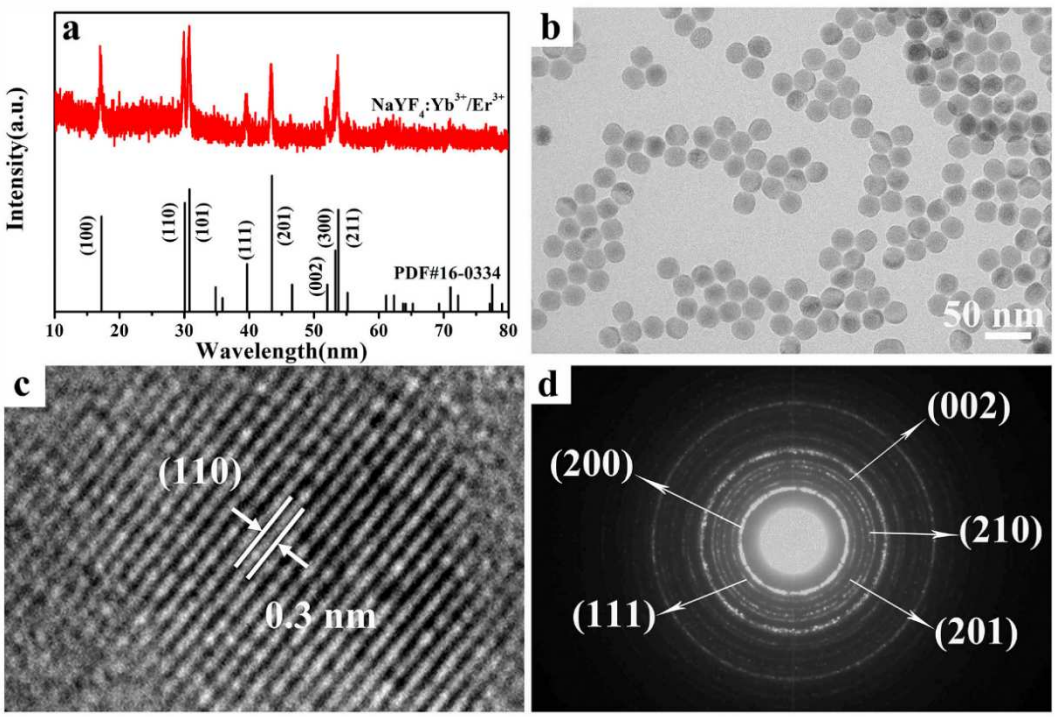

Figure 1 the XRD pattern (a), TEM image (b), high resolution TEM image (c) and selected area electron diffraction pattern (d) of the prepared $NaYF_4$: Yb^{3+}, Er^{3+} NPs.

The SEM image of OPC-I~III were presented in the Figure 2 (a) and the Figure S1~2 of supporting information, respectively. The silica microspheres form an ordered face centered cubic (fcc) arrangement with the close packed 111 plane parallel to Q substrate. After sintering of the silica OPCs with the infiltration of $HAuCl_4$ solution, the structure of Au/ OPC-I~III hybrids was characterized by the SEM, as shown in Figure 2 (b) and Figure S1~2. The bright spots in the Fig. 2 (b) and Fig. S1~2 of supporting information are the Au NPs with the irregular shape, and the homogeneous distribution of Au NPs was observed in the positions of OPCs voids. The size

distribution histogram of Au NPs was shown in the insert of Fig. 2 (b). It is clear that the sizes of Au NPs were in the region of 10-100 nm and average size was about 53 nm. The TEM images and EDX pattern of Au/OPC-I~III hybrids were used to further investigate the formation of Au/OPC-I~III hybrid structures and existence of Au NPs, as shown in Fig. 2 (c) and Fig. S1~2. The silica microspheres surface attached lots of small continuous bright spots (such as in the red circles) and some clear bigger bright spots. The larger Au island NPs and a layer of Au continuous film were formed on the surface of silica microspheres. These bright spots were verified as the Au element by the EDX pattern (Fig. 2 (c)). The SEM micrograph of Au NPs on the Q substrate was showed in the Figure S3 (a) of supporting information. It's noted that the size of Au NPs is in the region of 60-200 nm. Compared with the Au NPs on the OPC-I~III, the size of Au NPs on the Q substrate is lager, which suggested that SiO_2 microspheres of OPCs limited the growth of Au NPs. Figure 2 (d)-(f) and Figure S1~2 exhibited the SEM images of $NaYF_4$: Yb^{3+}, Er^{3+} NPs deposited on surface of OPC-I~III, Au/OPC-I~III and Q substrate, respectively. It is obvious that the surface and voids of OPC-I~III, Au/OPC- I~III and Q substrate were covered by a dense single layer of $NaYF_4$:Yb^{3+}, Er^{3+} NPs.

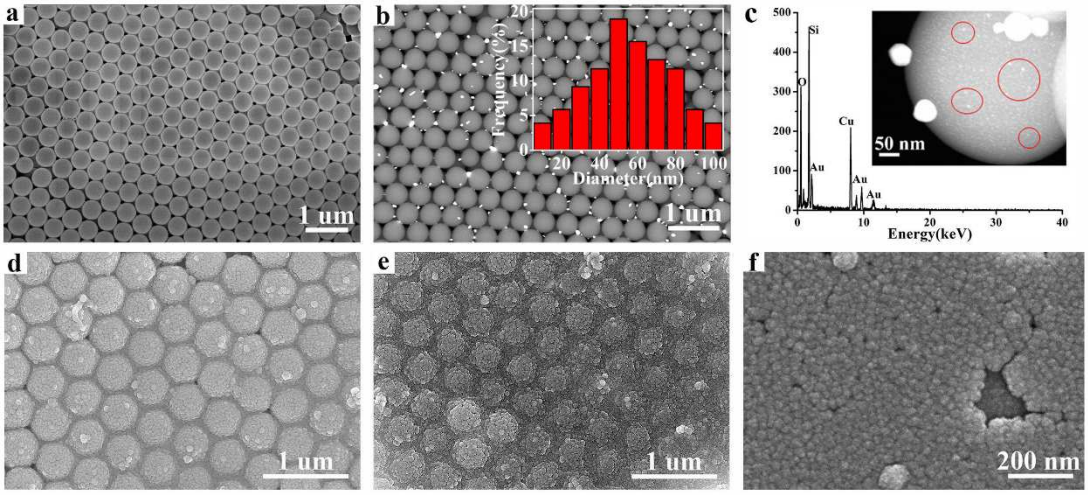

Figure 2 the SEM images of OPC-III (a) and Au/OPC-III hybrids (b); the insert in the (b) is the size distribution histogram of Au NPs; the EDX pattern (c) of the Au/OPC-III hybrids; the insert in the (c) is the TEM image of Au/OPC-III hybrids; the SEM images of $NaYF_4$:Yb^{3+}, Er^{3+} NPs deposited on the OPC-III (d), Au/OPC-III substrate (e) and Q substrate (f).

The absorption spectrum of Au NPs on the Q substrate is shown in the Figure S3 (b). It is clear that an obvious peak centered at 530 nm was exhibited in the absorption curve, which arises from the LSPR of Au NPs. Figure 3 presented the absorption spectra of OPC-I, OPC-II, OPC-III without and with Au NPs. Absorption curves of OPC-I~III showed an obvious photonic band gaps located at 561, 672 and 996 nm, respectively, which were overlapped with the green and red UC emission peaks of Er^{3+} and excitation wavelength of 980 nm, respectively. It is noted that the silica microsphere size would affect the position of photonic band gap of OPCs. Theoretically, Bragg's law: $\lambda=1.633D(n^2_{eff} - \sin^2\theta)$ could be used for calculating the position of photonic band gaps. According to the equation, the photonic band gaps of OPC-I~III are calculated as the 550, 659 and 1011 nm, respectively. Position of photonic band gap shifts to the long wavelength with the increasing size of silica microsphere. The calculation value of photonic band gap is consistent with the measurement value. After sintering OPC-I~III samples with the infiltration of $HAuCl_4$

solutions, the photonic band gaps position of Au/OPC-I~III hybrids shifted slightly to the shorter wavelength, and the photonic band gaps position of Au/OPC-I~III hybrids were located at the 538, 650 and 970 nm, respectively. The blue shift of photonic band gap may be due to the shrinking of microspheres and refractive index changing of Au/OPC-I~III structure. As can be seen in the Figure 3, the absorption curve of Au/OPC-II~III exhibited another peak centered at about 520 nm in contrast to the OPC-II~III, arising from Au NPs surface plasmon absorption. For the position of photonic band gap, OPC-I substrate is consistent with the LSPR of Au NPs, thus the absorption curve of Au/OPC-I only showed an absorption peak at the 538 nm.

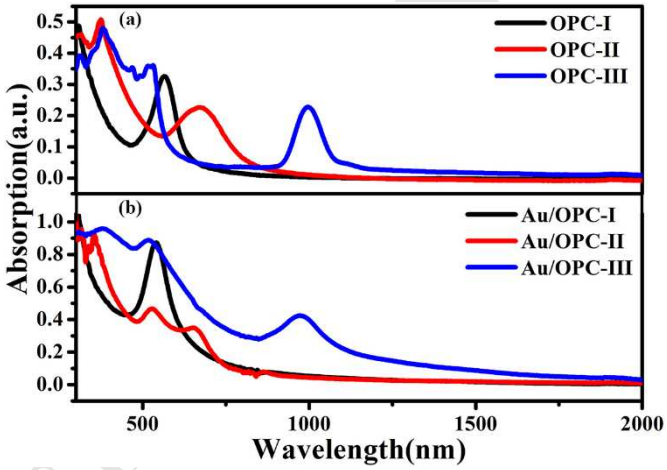

Figure 3 Absorption spectra of OPC-I~III (a) and Au/OPC-I~III hybrids (b)

3.2 The UC emission enhancement of $NaYF_4$:Yb^{3+}, Er^{3+} NPs by the Au/OPC-I~III hybrids

The UC emission spectra of $NaYF_4$: Yb^{3+}, Er^{3+} NPs deposited on the various templates were shown in Figure 4 excited at the 980 nm. All the UC photoluminescence spectra exhibited the obvious green emission peaks at 525, 545 nm and a red emission peak at 660 nm of Er^{3+} ions, which arise from the electronic

transition of $^2H_{11/2}\rightarrow{}^4I_{15/2}$, $^4S_{3/2}\rightarrow{}^4I_{15/2}$ and $^4F_{9/2}\rightarrow{}^4I_{15/2}$, respectively. There is an exponential relationship between UC emission intensity (I) and pump power (P) in the UC emission process of $NaYF_4$:Yb^{3+}, Er^{3+} NPs, which can be expressed as the $I=P^n$. The n value in the equation is the number of absorbed infrared photons from ground state to excited state required for an UC visible photon emission. Figure 5 is a log-log spectrum of UC emission intensity as the function of the pump power on the Q, Au/Q, OPC-III and Au/OPC-III substrates. The dependence of pump power and UC luminescence of $NaYF_4$:Yb^{3+}, Er^{3+} NPs on the OPC-I, Au/OPC-I, OPC-II and Au/OPC-II substrate are presented in Figure S4. It is clear from the Figure 5 and Figure S4 that the n value of $NaYF_4$:Yb^{3+}, Er^{3+} on the four templates for 545 and 660 nm reveals that the two-photon UC emission processes were involved for the green and red UC emissions. To better understand UC emission mechanisms of $NaYF_4$:Yb^{3+}, Er^{3+} NPs under the excitation of 980 nm, the energy transfer between Yb^{3+} ions and Er^{3+} ions was shown in Figure 6. Ground state Yb^{3+} ions absorb 980 nm excitation light, resulting in the transition from the $^2F_{7/2}$ to excited $^2F_{5/2}$ state. The absorption cross section of Yb^{3+} ions at 980 nm excitation light are larger than Er^{3+} ions. The Yb^{3+} ions served as sensitizer transfer their absorbed energy to adjacent Er^{3+} ions, and the Er^{3+} ions are excited from $^4I_{15/2}$ ground state to excited $^4I_{11/2}$ state. Subsequently, the higher $^4F_{7/2}$ excited state of Er^{3+} ions are populated due to the successive energy transfer from the Yb^{3+} ions to Er^{3+} ions in the excited $^4I_{11/2}$ state. The $^4F_{7/2}$ excited state of Er^{3+} ions are non-radiatively relaxed to the $^2H_{11/2}$ and $^4S_{3/2}$ states. Excited Er^{3+} ions in the $^2H_{11/2}$ and $^4S_{3/2}$ state are jumped back to $^4I_{11/2}$ state, leading to green UC

emission at the 525 and 545 nm, respectively. As the electrons of Er^{3+} ions in the $^4I_{11/2}$ state undergo non-radiative relaxation to the lower $^4I_{13/2}$ state, the $^4I_{13/2}$ state of Er^{3+} ions can be excited to the $^4F_{9/2}$ state due to the energy transfer of Yb^{3+} ions. Additionally, the $^4F_{9/2}$ state of Er^{3+} ions are populated by the non-radiative relaxation from higher the $^2H_{11/2}$ and $^4S_{3/2}$ states, The radiative transition from the $^4F_{9/2}$ excited state to $^4I_{15/2}$ ground state of Er^{3+} ions result in the red UC emission located at the 660 nm.

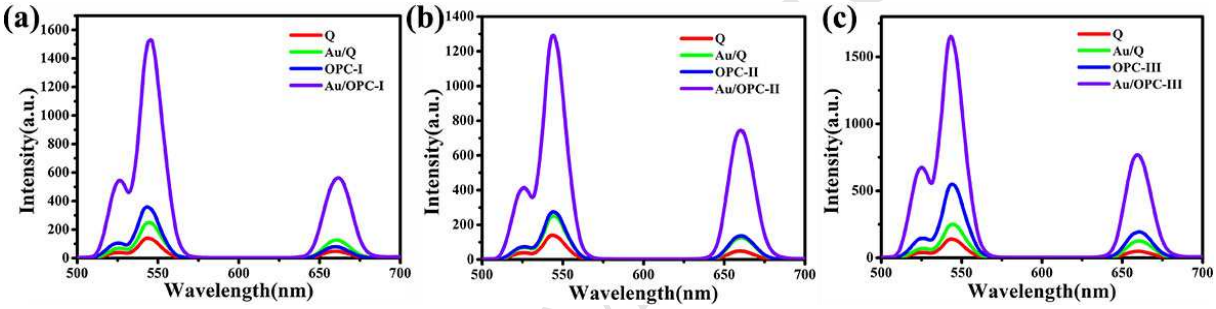

Figure 4 the UC emission spectra of $NaYF_4$:Yb^{3+}, Er^{3+} NPs deposited on the surface of Q, Au/Q, OPC-I, Au/OPC-I (a), Q, Au/Q, OPC-II, Au/OPC-II (b) and Q, Au/Q, OPC-III, Au/OPC-III (c) under the excitation of 980 nm.

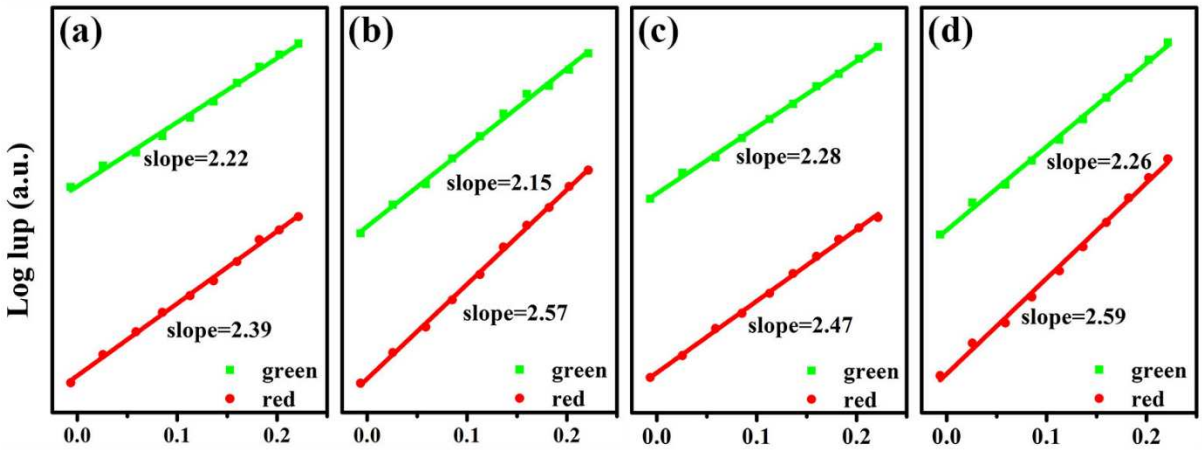

Figure 5 the dependence of pump power of 980 nm excitation light on the 545 and 660 nm UC emission intensity of $NaYF_4$:Yb^{3+}, Er^{3+} NPs deposited on Q (a), Au/Q (b), OPC-III (c) and Au/OPC-III (d) substrates.

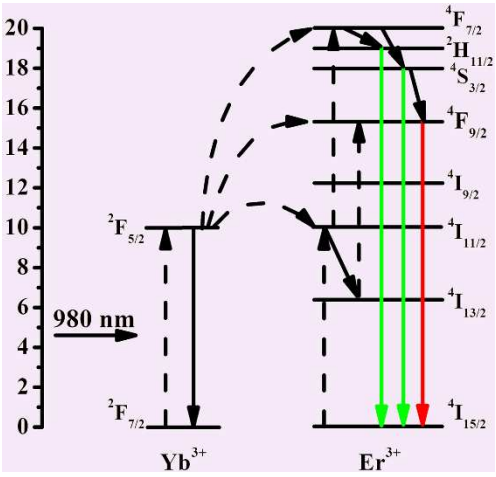

Figure 6 the UC emission mechanism of $NaYF_4$:Yb^{3+}, Er^{3+} NPs upon the 980 nm excitation.

The UC photoluminescence of $NaYF_4$:Yb^{3+}, Er^{3+} NPs on various substrate presented the different emission intensity. The UC emission intensity on the various substrates was enhanced in comparison with that of $NaYF_4$:Yb^{3+}, Er^{3+} NPs on the Q substrate. The corresponding enhancement factor (EF) of UC emission has been obtained, as shown in the Figure 7. The EF in Figure 7 (a) is the ratio of UC emission intensity of $NaYF_4$:Yb^{3+}, Er^{3+} NPs on the Au/Q, OPC-I~III substrate to that of $NaYF_4$:Yb^{3+}, Er^{3+} NPs on the Q substrate, respectively. Owing to the substrates coated by the $NaYF_4$:Yb^{3+}, Er^{3+} NPs with the same amount. Thus the influence of thickness and quantity of $NaYF_4$:Yb^{3+}, Er^{3+} NPs on the UC emission intensity could be avoided. As seen in Figure 7, the EF of green and red UC emission on the OPC-I is 2.6 and 1.7, respectively, and the corresponding EF values of red and green emission of $NaYF_4$:Yb^{3+}, Er^{3+} NPs on the OPC-II substrate is 2.8 and 2, respectively. For the OPC-III substrate, the EF values at green and red emission were about 4. It can be seen that the UC emission of the $NaYF_4$:Yb^{3+}, Er^{3+} NPs was enhanced on the surface of photonic crystal, attributing to the excitation enhancement caused by the silica

microspheres induced the excitation light scattering. The electric field intensity of OPC-I~III substrates along the polarization of X-axis and Y-axis was simulated with the excitation light of 980 nm, showing the enhancement of electric field intensity, as shown in Figure 8 and Figure S5. The EF values of green and red UC emissions of $NaYF_4$:Yb^{3+}, Er^{3+} NPs on the surface of OPC-III are larger than these of $NaYF_4$:Yb^{3+}, Er^{3+} NPs on the OPC-I~II. The photonic band gap of OPC-III is overlapped with the 980 nm excitation light, which can couple well with the excitation light of 980 nm. Thus the larger enhancement of excitation field can obtained, resulting in the larger UC emission enhancement on the OPC-III. Selective green UC enhancement of $NaYF_4$:Yb^{3+}, Er^{3+} NPs on the OPC-I was presented in contrast to the red UC emission. For the OPC-II substrate, the red UC emission enhancement of $NaYF_4$:Yb^{3+}, Er^{3+} NPs is larger than its green UC emission. Photons cannot be propagated in the wavelength range of photonic band gap. The selective enhancement of UC of $NaYF_4$:Yb^{3+}, Er^{3+} NPs on the OPC-I and OPC-II is due to the Bragg diffraction of photonic band gap [24, 30].

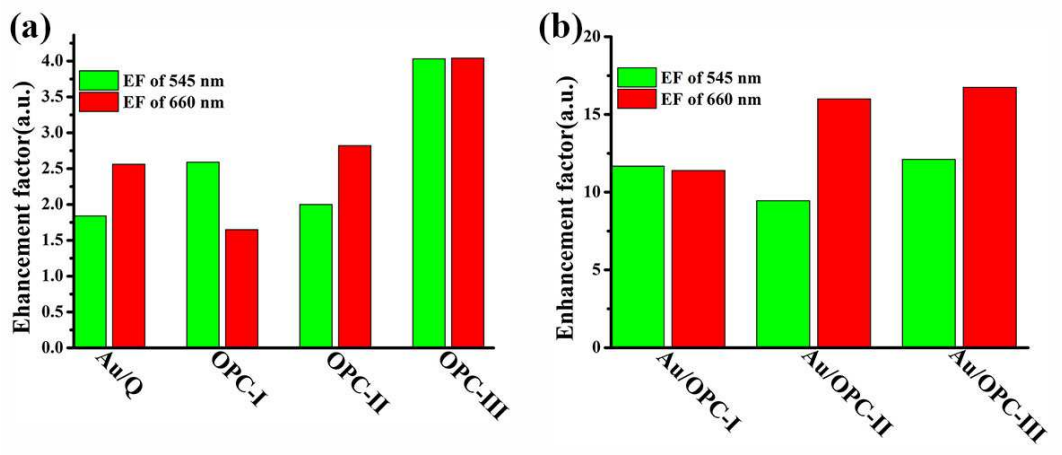

Figure 7 the UC emission enhancement factor of $NaYF_4$:Yb^{3+}, Er^{3+} NPs on the Au/Q, OPC-I, OPC-II and OPC-III substrates (a) and Au/OPC-I, Au/OPC-II and Au/OPC-III substrates (b);

The UC emission EF of 545 and 660 nm of $NaYF_4$:Yb^{3+}, Er^{3+} NPs on the Au/Q substrate increased by 1.8 and 2.6 folds in contrast to the Q substrate, respectively. It's well-known that the LSPR of Au NPs can improve UC luminescence intensity due to the emission rate increasing or excitation field enhancement [31, 32]. The investigation of the enhancement mechanism of $NaYF_4$ NPs on the Au/OPC hybrid was carried out. The decay curves of NPs on the Q and Au/Q substrates were shown in the Figure 9. The decay lifetimes of the UC emission of $NaYF_4$ NPs on the Q and Au/Q substrates exhibited no change, indicating decay rate increasing has no effect on the UC emission of $NaYF_4$ NPs on the Au/Q substrate. The electric field intensity and distribution of the Au/Q substrate along the polarization of X-axis and Y-axis was simulated by finite-difference time-domain (FDTD) software excited at 980 nm as shown in Figure 8 (d) and Figure S5. The hot spots were formed around the Au NPs regarding of the polarization direction. These results indicated that the enhancement of UC emission on the Au/Q template could be from the electric field enhancement around Au NPs. The relationship between the UC intensity (I) and the excitation field intensity(E) can be expressed as the $I \propto E^n$, where the n is the photons number. The n value of red UC emission is larger that of green UC emission, as shown in Figure 5. Thus the enhancement factor of red UC emission is larger than that of the green UC emission.

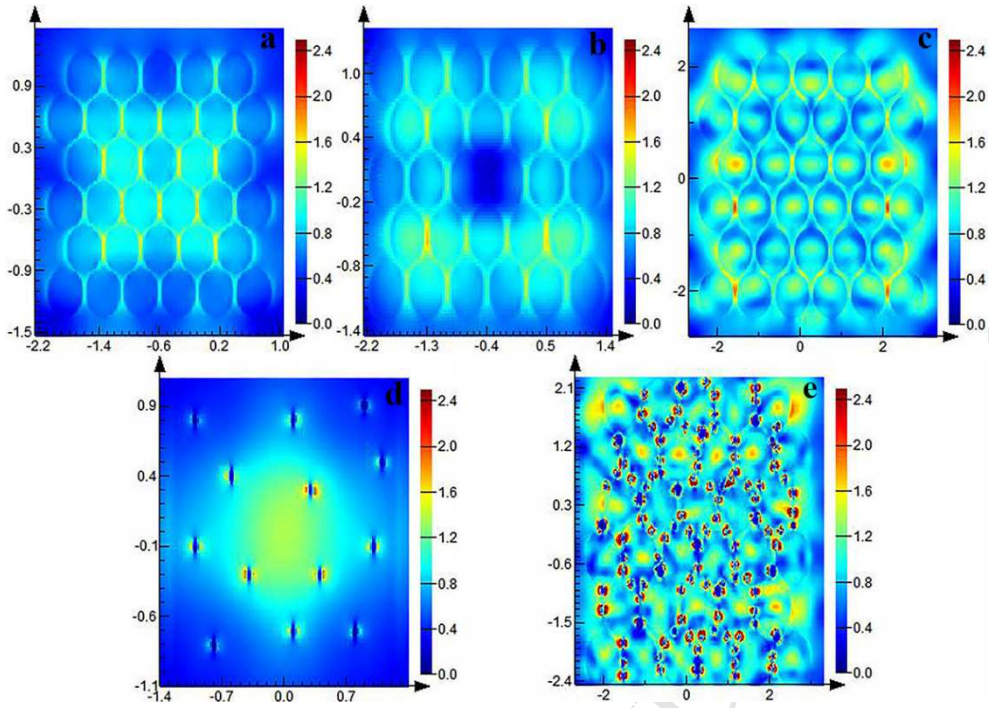

Figure 8 the simulated electric field of OPC-I (a), OPC-II (b), OPC-III substrate (c), Au/Q substrate (d) and Au/OPC-III hybrids (e) along the polarization of X-axis under the excitation of 980 nm.

The UC emission spectra of $NaYF_4$ NPs/Au/OPC-I~III hybrids presented in the Fig. 4 exhibited the further UC emission enhancement comparing with these of $NaYF_4$:Yb^{3+}, Er^{3+} NPs on OPC-I~III or Au/Q substrates. The corresponding EF were shown in the Figure 7 (b). The EF of green and red UC emissions on the surface of on the Au/OPC-I hybrid is 11.7 and 11.4, respectively. On the Au/OPC-II, the EF of green and red UC emissions is 9.5 and 16 folds, respectively. For Au/OPC-III hybrid, the EF of green and red UC emission of $NaYF_4$:Yb^{3+}, Er^{3+} NPs is 12.11 and 16.8 folds, respectively. It is clear that the UC emission intensity of $NaYF_4$:Yb^{3+}, Er^{3+} NPs on the Au/OPC-I~III hybrid is larger than the total sum on the OPC and Au/Q substrate, which indicated that the coupling of OPC and Au NPs improve greatly the UC emission intensity in comparison with separate OPC or Au/Q substrate. As shown in

Figure 9 (b), the decay lifetimes of the green and red UC emission of $NaYF_4$ NPs on the Au/OPC-I~III hybrids have no significant difference in contrast to the OPC and Au/Q substrate, which indicated the enhanced UC emission on the Au/OPC-I~III hybrids was not from the emission rate increasing. As presented in Figure 8 (e), for Au/OPC hybrid structure, the simulated electric field distribution and intensity is larger in compared with separated OPC or Au NPs substrates. Thus, the UC emission enhancement of $NaYF_4$:Yb^{3+}, Er^{3+} NPs on the Au/OPC-I~III hybrids arise mainly from the enhancement of excited electric field.

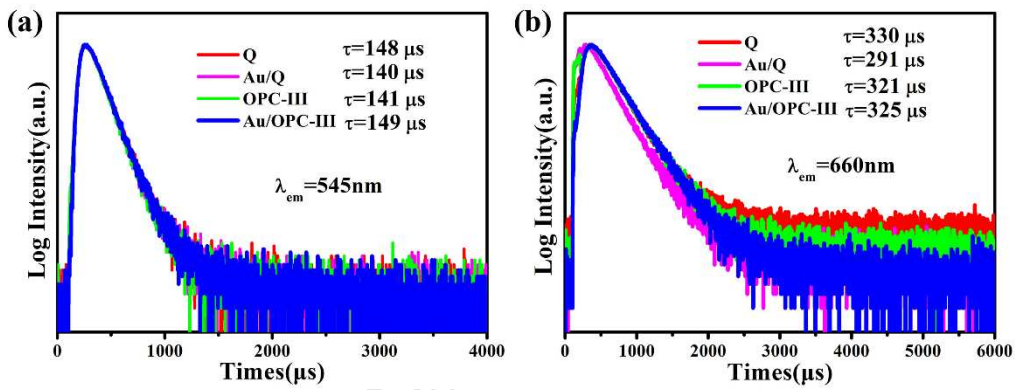

Figure 9 Decay curves of 545 (a) and 660 nm (b) UC emission of $NaYF_4$:Yb^{3+}, Er^{3+} NPs on the Q, Au/Q, OPC-III and Au/OPC-III substrates.

3.3 Detection enhancement of RhB by the $NaYF_4$/Au/OPC-III hybrid structure

The UC emission of $NaYF_4$:Yb^{3+}, Er^{3+} NPs on the prepared Au/OPC-I~III could be improved, which can solve its low UC emission. The $NaYF_4$/Au/OPC-III NPs can served as a solid-state sensor to detect the RhB through the change of UC emission intensity of $NaYF_4$:Yb^{3+}, Er^{3+} NPs. Figure 10 depicts the absorption spectra of the RhB on the Q and $NaYF_4$:Yb^{3+}, Er^{3+}/Au/OPC-III hybrid substrates, respectively. The absorption peak at the 556 nm is from the absorption of the RhB, which is overlapped

with the green UC emission peak of $NaYF_4$:Yb^{3+}, Er^{3+} NPs. Thus, the energy transfer from the $NaYF_4$:Yb^{3+}, Er^{3+} NPs to the RhB may take place.

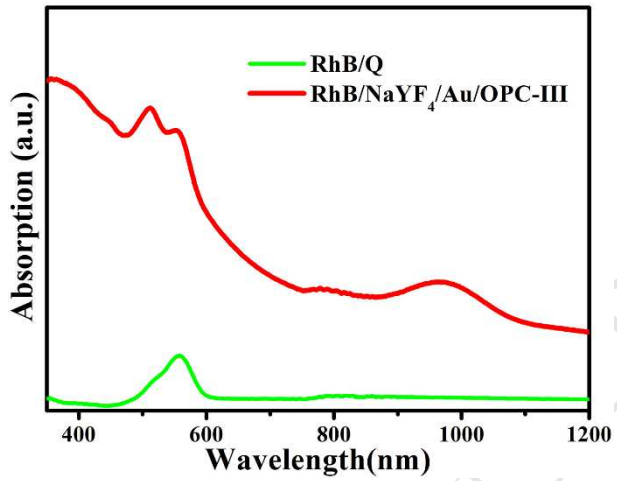

Figure 10 the absorption spectra of RhB on the Q and $NaYF_4$/Au/OPC-III hybrids

The UC emission of $NaYF_4$:Yb^{3+}, Er^{3+} NPs on the Q and Au/OPC-III hybrid substrates as the function of RhB concentration are shown in Figure 11 (a) and (b) under the excitation of 980 nm, respectively. For the $NaYF_4$:Yb^{3+}, Er^{3+} NPs on the Q and Au/OPC-III hybrid substrates, the decreasing of green UC emission and no changing of red UC emission was observed with increasing the RhB concentration. It is interesting that for the RhB on the $NaYF_4$:Yb^{3+}, Er^{3+}/Au/OPC-III hybrids, the emission peak located at the 581 nm form the RhB was observed. However, the 581 nm emission peak of the RhB was not observed obviously for the RhB on the $NaYF_4$:Yb^{3+},Er^{3+}/Q substrate. The direct contact between the Au NPs and RhB can influence the luminescence of RhB, which can result in the luminescence quenching or enhancement. In present work, the luminescence enhancement of RhB was observed. If the luminescence enhancement of RhB is from the influence of Au NPs, the decreasing of green UC emission cannot observed with increasing the RhB

concentration, which is inconsistent with the results. Therefore, the influence of the direct contact between the Au NPs and RhB on the luminescence quenching or enhancement of RhB can be removed. The green UC emission is overlapped with the absorption of RhB, which demonstrated the energy transfer from the $NaYF_4$:Yb^{3+}, Er^{3+} NPs to the RhB can occur. Therefore, the green UC emission intensity was decreased because of the energy transfer from the $NaYF_4$:Yb^{3+}, Er^{3+} NPs to the RhB. The UC emission enhancement of $NaYF_4$:Yb^{3+}, Er^{3+} NPs induced by the Au/OPC-III hybrids enhance improve the energy transfer from $NaYF_4$:Yb^{3+}, Er^{3+} NPs to RhB. Thus the 581 nm emission of the RhB was observed for the RhB on the $NaYF_4$:Yb^{3+}, Er^{3+}/Au/OPC-III hybrid in contrast to the $NaYF_4$:Yb^{3+}, Er^{3+}/Q substrate.

The green UC emission intensity of the $NaYF_4$:Yb^{3+}, Er^{3+} NPs on the Q and Au/OPC-III hybrid substrates are shown in Figure 11 (c) and (d) as the function of the RhB concentration, respectively. For the $NaYF_4$:Yb^{3+}, Er^{3+} NPs on the Q substrate, the linear relationship coefficient of R^2 of the green UC emission intensity is 0.975 with the RhB concentration from 0 to 0.875 mM and the sensitivity is 0.033 μM^{-1}. The linear relationship coefficient of higher R^2 of the green UC emission intensity of $NaYF_4$:Yb^{3+}, Er^{3+} NPs on the Au/OPC-III hybrids is 0.997 with a sensitivity of 1.15 μM^{-1}. The results suggested that the $NaYF_4$ NPs with the UC emission as a solid-state sensor can be used for detecting RhB. The UC emission enhancement of NPs caused by Au/OPC-III hybrids improve the detection sensitivity of RhB. For the sensor, the limit of detection (LOD) is one of the essential sensing parameters besides the sensitivity [33, 34]. The LOD can be expressed by the 3s/m equation, where the s and

m is the standard deviation and the slope of line plotted by the ratio of luminescence intensity of acceptor (RhB) to that of donor($NaYF_4$:Yb^{3+},Er^{3+}) [17, 35], respectively. For the RhB on the $NaYF_4$:Yb^{3+}, Er^{3+}/Q substrate, there was no the 581 nm emission of the RhB. Therefore, the LOD could not be obtained. For the RhB on the $NaYF_4$:Yb^{3+}, Er^{3+}/Au/OPC-III hybrid, the 581 nm emission intensity of the RhB was increased with the increasing of RhB concentration. The result means that the $NaYF_4$ NPs on the Au/OPC hybrid is beneficial to detect the RhB. To obtain the LOD parameter, the ratio of 581 nm emission intensity (I_{581}) RhB to the 545 nm green UC emission intensity (I_{545}) is calculated as the function of the RhB concentration on the Au/OPC-III hybrid as shown in Figure 11 (e). The I_{581}/ I_{545} ratio was increased with RhB concentration increasing from 0.175 to 0.875 mM and show the good linear relationship. The LOD is calculated as the 164 μM.

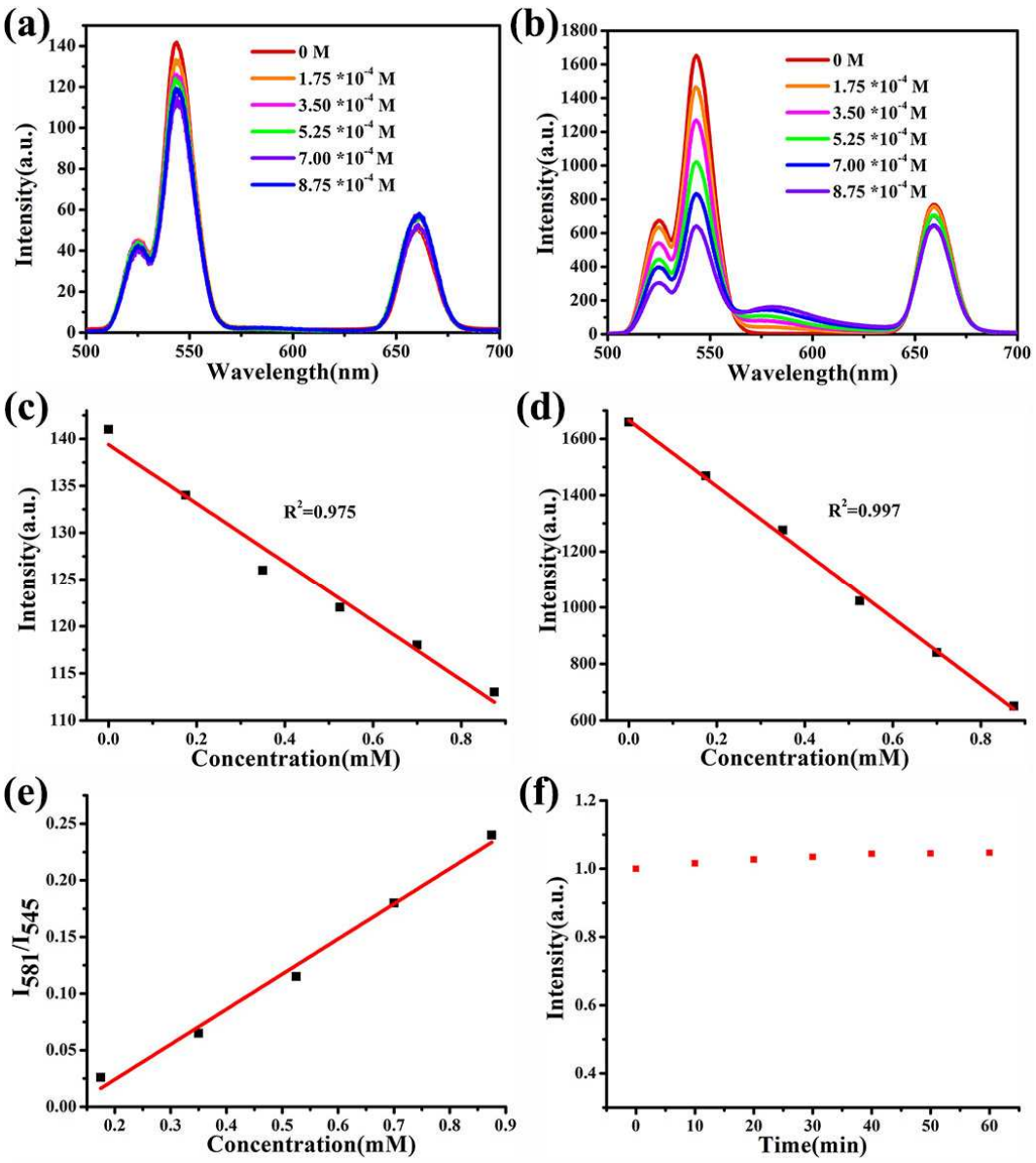

Figure 11. the UC emission of $NaYF_4$:Yb^{3+}, Er^{3+} NPs deposited on the Q (a) and Au/OPC-III substrates (b) as the function of RhB concentration; corresponding linear relationship of green UC emission intensity with the increasing of RhB concentration on the Q (c) and Au/OPC-III substrate (d); the calibration curve of I_{581}/I_{545} versus RhB concentration on $NaYF_4$/Au/OPC-III hybrid (e); the stability curves of RhB/$NaYF_4$/Au/OPC-III hybrid (f).

For the RhB detection, it is necessary to investigate the photo-stability of the sensor. Figure 11 (f) is the changing of green UC emission intensity of RhB/$NaYF_4$/Au/OPC-III as the function of the time under the continuous illumination

of a 980 nm laser. The green emission intensity at 0 min is denoted as 1. It is clear that the green UC emission intensity is not more than 1.05 under the continuous illumination of a 980 nm laser for 1 h, exhibiting the unchanging. The result indicated the $NaYF_4$ NPs/Au/OPC-III hybrid is stable as a solid-state sensor of the RhB detection, which may be used for the detecting RhB in water or food.

Conclusions

The hybrids constructed with the Au NPs and SiO_2 opal photonic crystals were prepared through a simple approach. $NaYF_4$:Yb^{3+}, Er^{3+} NPs were deposited on the surface of Au/opal hybrids. The influence of coupling metal NPs with photonic crystals on the UC luminescence of $NaYF_4$:Yb^{3+}, Er^{3+} NPs has been investigated. The enhanced UC emission of $NaYF_4$:Yb^{3+}, Er^{3+} NPs excited at 980 nm can be observed based on the coupling of Au NPs and photonic crystals, and the maximum UC emission enhancement was about 17-fold. The UC luminescence enhancement on the Au/OPC hybrid mainly arise from the enhancement of excited electric field. The $NaYF_4$ UC luminescence NPs can served as a solid-state sensor to detect the RhB through the change of UC emission intensity of $NaYF_4$:Yb^{3+}, Er^{3+} NPs. Comparing with the pure $NaYF_4$:Yb^{3+}, Er^{3+} NPs, the sensor of $NaYF_4$:Yb^{3+}, Er^{3+} NPs on the Au/OPC hybrid was improved, existing a low detection limit of 164 μM and a high sensitivity of 1.15 μM^{-1}. For the $NaYF_4$:Yb^{3+}, Er^{3+} NPs deposited on the Au/opal hybrids, the detection sensitivity of RhB was increased by about 35-factors.

Acknowledgments

This work was supported by the National Natural Science Foundation of China

(51762029, 11674137), and the Applied Basic Research Key Program of Yunnan Province (2018FA026).

References

[1] M. Oplatowska, C.T. Elliott, Development and validation of rapid disequilibrium enzyme-linked immunosorbent assays for the detection of Methyl Yellow and Rhodamine B dyes in foods, Analyst, 136 (2011) 2403-2410.

[2] C.S. Guo, J.A. Xu, Y. He, Y.A. Zhang, Y.Q. Wang, Photodegradation of rhodamine B and methyl orange over one-dimensional TiO2 catalysts under simulated solar irradiation, Appl Surf Sci, 257 (2011) 3798-3803.

[3] C. Wang, F.S. Cheng, Y.H. Wang, Z.J. Gong, M.K. Fan, J.M. Hu, Single point calibration for semi-quantitative screening based on an internal reference in thin layer chromatography-SERS: the case of Rhodamine B in chili oil, Anal Methods-Uk, 6 (2014) 7218-7223.

[4] S.D. Richardson, C.S. Willson, K.A. Rusch, Use of rhodamine water tracer in the marshland upwelling system, Ground Water, 42 (2004) 678-688.

[5] D. Kornbrust, T. Barfknecht, Testing of 24 Food, Drug, Cosmetic, and Fabric Dyes in the In Vitro and the In Vivo/ In Vitro Rat Hepatocyte Primary Culture/ DNA Repair Assays, 7 (1985).

[6] R. Jain, M. Mathur, S. Sikarwar, A. Mittal, Removal of the hazardous dye rhodamine B through photocatalytic and adsorption treatments, J Environ Manage, 85 (2007) 956-964.

[7] H. Wang., X. Guo., S. Fu., T. Yang., Y. Wen., H. Yang., Optimized core–shell Au@Ag nanoparticles for label-free Raman determination of trace Rhodamine B with cancer risk in food product, Food Chemistry, 188 (2015) 137-142.

[8] H.Y. Li, N.J. Li, J. Jiang, D.Y. Chen, Q.F. Xu, H. Li, J.H. He, J.M. Lu, Molecularly imprinted magnetic microparticles for the simultaneous detection and extraction of Rhodamine B, Sensor Actuat B-Chem, 246 (2017) 286-292.

[9] L.M. Xu, J. Kang, Y.M. Zeng, H.Z. Kang, Rapid detection of Rhodamine B in raw paprika and other food based on SERS technique, Science and Technology of Food Industry, (2017) 238-243.

[10] P. Qi, Z.H. Lin, J.X. Li, C.L. Wang, W.W. Meng, H. Hong, X.W. Zhang, Development of a rapid, simple and sensitive HPLC-FLD method for determination of rhodamine B in chili-containing products, Food Chemistry, 164 (2014) 98-103.

[11] M. Soylak, Y.E. Unsal, E. Yilmaz, M. Tuzen, Determination of rhodamine B in soft drink, waste water and lipstick samples after solid phase extraction, Food Chem Toxicol, 49 (2011) 1796-1799.

[12] L. Zhang, P. Li, L. Luo, X. Bu, X. Wang, B. Zhao, Y. Tian, Sensitive Detection of Rhodamine B in Condiments Using Surface-Enhanced Resonance Raman Scattering (SERRS) Silver Nanowires as Substrate, Applied Spectroscopy, 71 (2017) 2395-2403.

[13] Q. Liu, Y. Sun, T. Yang, W. Feng, C. Li, F. Li, Sub-10 nm Hexagonal Lanthanide-Doped NaLuF4 Upconversion Nanocrystals for Sensitive Bioimaging in Vivo, Journal of the American Chemical Society, 133 (2011) 17122-17125.

[14] H.Q. Wang, M. Batentschuk, A. Osvet, L. Pinna, C.J. Brabec, Rare-Earth Ion Doped Up-Conversion Materials for Photovoltaic Applications, Adv Mater, 23 (2011) 2675-2680.

[15] V. Kumar, A. Pandey, S.K. Swami, O.M. Ntwaeaborwa, H.C. Swart, V. Dutta, Synthesis and characterization of Er^{3+}-Yb^{3+} doped ZnO upconversion nanoparticles for solar cell application, J Alloy

Compd, 766 (2018) 429-435.

[16] H. Chen, X.S. Zhai, D. Li, L.L. Wang, D. Zhao, W.P. Qin, Water-soluble Yb^{3+}, Tm^{3+} codoped $NaYF_4$ nanoparticles: Synthesis, characteristics and bioimaging, J Alloy Compd, 511 (2012) 70-73.

[17] S.J. Liu, Y.J. Li, C. Zhang, L. Yang, T.T. Zhao, R.L. Zhang, C.L. Jiang, Upconversion color tuning in Ce^{3+}-doped $LiYF_4$:Yb^{3+}/Ho^{3+}@$LiYF_4$ nanoparticles towards ratiometric fluorescence detection of chromium (III), J Colloid Interf Sci, 493 (2017) 10-16.

[18] Y.Q. Zhang, S. Xu, X.P. Li, J.S. Zhang, J. Sun, L.L. Tong, H. Zhong, H.P. Xia, R.N. Hua, B.J. Chen, Improved LRET-based detection characters of Cu^{2+} using sandwich structured $NaYF_4$@$NaYF_4$:Er^{3+}/Yb^{3+}@$NaYF_4$ nanoparticles as energy donor, Sensor Actuat B-Chem, 257 (2018) 829-838.

[19] P. Alonso-Cristobal, P. Vilela, A. El-Sagheer, E. Lopez-Cabarcos, T. Brown, O.L. Muskens, J. Rubio-Retama, A.G. Kanaras, Highly Sensitive DNA Sensor Based on Upconversion Nanoparticles and Graphene Oxide, Acs Appl Mater Inter, 7 (2015) 12422-12429.

[20] R. Niepelt, U.C. Schroder, J. Sommerfeld, I. Slowik, B. Rudolph, R. Moller, B. Seise, A. Csaki, W. Fritzsche, C. Ronning, Biofunctionalization of zinc oxide nanowires for DNA sensory applications, Nanoscale Res Lett, 6 (2011).

[21] B. Wu, Z.Q. Cao, Q. Zhang, G.J. Wang, NIR-responsive DNA hybridization detection by high efficient FRET from 10-nm upconversion nanoparticles to SYBR green I, Sensor Actuat B-Chem, 255 (2018) 2853-2860.

[22] G.Y. Lee, K. Jung, H.S. Jang, J. Kyhm, I.K. Han, B. Park, H. Ju, S.J. Kwon, H. Ko, Upconversion luminescence enhancement in plasmonic architecture with random assembly of metal nanodomes, Nanoscale, 8 (2016) 2071-2080.

[23] Y.D. Wang, Z.W. Yang, Y.J. Ma, Z.Z. Chai, J.B. Qiu, Z.G. Song, Upconversion emission enhancement mechanisms of Nd^{3+}-sensitized $NaYF_4$: Yb^{3+}, Er^{3+} nanoparticles using tunable plasmonic Au films: plasmonicinduced excitation, radiative decay rate and energy-transfer enhancement, J Mater Chem C, 5 (2017) 8535-8544.

[24] W.N. Zhang, J. Li, H.X. Lei, B.J. Li, Plasmon-Induced Selective Enhancement of Green Emission in Lanthanide-Doped Nanoparticles, Acs Appl Mater Inter, 9 (2017) 42935-42942.

[25] Z. Yin, Y.S. Zhu, W. Xu, J. Wang, S. Xu, B. Dong, L. Xu, S. Zhang, H.W. Song, Remarkable enhancement of upconversion fluorescence and confocal imaging of PMMA Opal/$NaYF_4$:Yb^{3+}, Tm^{3+}/Er^{3+} nanocrystals, Chem Commun, 49 (2013) 3781-3783.

[26] J.Y. Liao, Z.W. Yang, H.J. Wu, D. Yan, J.B. Qiu, Z.G. Song, Y. Yang, D.C. Zhou, Z.Y. Yin, Enhancement of the up-conversion luminescence of Yb^{3+}/Er^{3+} or Yb^{3+}/Tm^{3+} co-doped $NaYF_4$ nanoparticles by photonic crystals, J Mater Chem C, 1 (2013) 6541-6546.

[27] B. Shao, Z.W. Yang, Y.D. Wang, J. Li, J.Z. Yang, J.B. Qiu, Z.G. Song, Coupling of Ag Nanoparticle with Inverse Opal Photonic Crystals as a Novel Strategy for Upconversion Emission Enhancement of $NaYF_4$: Yb^{3+}, Er^{3+} Nanoparticles, Acs Appl Mater Inter, 7 (2015) 25211-25218.

[28] F. Wang, R.R. Deng, X.G. Liu, Preparation of core-shell $NaGdF_4$ nanoparticles doped with luminescent lanthanide ions to be used as upconversion-based probes, Nat Protoc, 9 (2014) 1634-1644.

[29] Z.W. Yang, X.G. Huang, G. Yang, Q. Xie, B. Li, J. Zhou, L.T. Li, Preparation and photonic bandgap properties of lead lanthanum titanate inverse opal photonic crystals, J Alloy Compd, 468 (2009) 295-298.

[30] W.B. Niu, L.T. Su, R. Chen, H. Chen, Y. Wang, A. Palaniappan, H.D. Sun, A.L.Y. Tok, 3-Dimensional photonic crystal surface enhanced upconversion emission for improved near-infrared

photoresponse, Nanoscale, 6 (2014) 817-824.

[31] W.H. Zhang, F. Ding, S.Y. Chou, Large Enhancement of Upconversion Luminescence of $NaYF_4$:Yb^{3+}/Er^{3+} Nanocrystal by 3D Plasmonic Nano-Antennas, Adv Mater, 24 (2012) Op236-Op241.

[32] S.J. Kwon, G.Y. Lee, K. Jung, H.S. Jang, J.S. Park, H. Ju, I. Han, H. Ko, A Plasmonic Platform with Disordered Array of Metal Nanoparticles for Three-Order Enhanced Upconversion Luminescence and Highly Sensitive Near-Infrared Photodetector, Adv Mater, 28 (2016) 7899-7909.

[33] J. Song, L. Xu, C.Y. Zhou, R.Q. Xing, Q.L. Dai, D.L. Liu, H.W. Song, Synthesis of Graphene Oxide Based CuO Nanoparticles Composite Electrode for Highly Enhanced Nonenzymatic Glucose Detection, Acs Appl Mater Inter, 5 (2013) 12928-12934.

[34] A. Umar, M.M. Rahman, S.H. Kim, Y.B. Hahn, Zinc oxide nanonail based chemical sensor for hydrazine detection, Chem Commun, (2008) 166-168.

[35] S. Xu, W. Xu, Y.F. Wang, S. Zhang, Y.S. Zhu, L. Tao, L. Xia, P.W. Zhou, H.W. Song, $NaYF_4$:Yb,Tm nanocrystals and TiO_2 inverse opal composite films: a novel device for upconversion enhancement and solid-based sensing of avidin, Nanoscale, 6 (2014) 5859-5870.

Highlights

1.The Au nanoparticles/opal photonic crystal hybrid was prepared by sintering method.

2.Upconversion emission enhancement of $NaYF_4$ nanoparticels has been largely improved.

3.The detection of Rhodamine B by $NaYF_4$:Yb^{3+}, Er^{3+} nanoparticles was realized.

4.The sensor sensitivity of $NaYF_4$ on the Au nanoparticles/opal hybrid was increased.